

# Hierarchical Turbulence and Geometry Modeling

Wang, Zhong-Nan; Tucker, Paul G.

DOI:

[10.2514/1.J062495](https://doi.org/10.2514/1.J062495)

License:

Creative Commons: Attribution (CC BY)

*Document Version*

Peer reviewed version

*Citation for published version (Harvard):*

Wang, Z-N & Tucker, PG 2023, 'Hierarchical Turbulence and Geometry Modeling: Case Study for Fan Stage Flows', *AIAA Journal*, vol. 61, no. 7, pp. 2824-2839. <https://doi.org/10.2514/1.J062495>

[Link to publication on Research at Birmingham portal](#)

## General rights

Unless a licence is specified above, all rights (including copyright and moral rights) in this document are retained by the authors and/or the copyright holders. The express permission of the copyright holder must be obtained for any use of this material other than for purposes permitted by law.

- Users may freely distribute the URL that is used to identify this publication.
- Users may download and/or print one copy of the publication from the University of Birmingham research portal for the purpose of private study or non-commercial research.
- User may use extracts from the document in line with the concept of 'fair dealing' under the Copyright, Designs and Patents Act 1988 (?)
- Users may not further distribute the material nor use it for the purposes of commercial gain.

Where a licence is displayed above, please note the terms and conditions of the licence govern your use of this document.

When citing, please reference the published version.

## Take down policy

While the University of Birmingham exercises care and attention in making items available there are rare occasions when an item has been uploaded in error or has been deemed to be commercially or otherwise sensitive.

If you believe that this is the case for this document, please contact [UBIRA@lists.bham.ac.uk](mailto:UBIRA@lists.bham.ac.uk) providing details and we will remove access to the work immediately and investigate.

# Hierarchical Turbulence and Geometry Modelling: A Case Study for Fan Stage Flows \*

Zhong-Nan Wang <sup>†</sup>

*University of Birmingham, Birmingham B15 2TT, England*

Paul G. Tucker <sup>‡</sup>

*University of Cambridge, Cambridge CB2 1PZ, England*

Flow separations occur in the tip region when the fan is operating at the approach condition. To reduce computational cost without degrading accuracy, the hierarchical modelling approach has been developed to predict such fan flow. This allows both flow and geometry to be treated with various fidelity levels in different zones. To be specific, this is achieved by zonalising Large-Eddy Simulation (LES) in the fan tip region and modelling downstream stators with low-order blade body forces. This approach provides an accurate and economical prediction of separated fan flows in the stage environment. The predicted fan wake profiles show a reasonably good agreement with the hot-wire measurements considering passage-to-passage variations. Finally, the simulation data are used to assess the isotropic turbulence hypothesis that is made on fan wake in low-order acoustics models.

## Nomenclature

$c$	=	chord, $m$
$u_i$	=	velocity in the $x_i$ direction, $m/s$
$u_\tau$	=	friction velocity, $\sqrt{\tau_w/\rho}$ , $m/s$
$E$	=	total internal energy, $J$
$f$	=	blending function for hybrid LES-RANS, -
$f_{b,i}$	=	blade body force in $x_i$ direction, $N/m^3$
$p$	=	pressure, $Pa$
$q_i$	=	heat conduction in the $x_i$ direction, $J/m^2$
$\rho$	=	density, $kg/m^3$
$\lambda$	=	blade blockage factor, -

---

\*part of this paper has been presented at AIAA AVIATION 2021 FORUM, August 2-6,2021, Virtual Event. Paper number: AIAA2021-2767

<sup>†</sup>Lecturer/Assistant Professor, College of Engineering and Physical Sciences, Birmingham; Visiting academic fellow, Department of Engineering, Cambridge, and Member AIAA. (corresponding author, email: z.n.wang@bham.ac.uk)

<sup>‡</sup>Rank Professor of Engineering, Department of Engineering, and Associate Fellow AIAA.

$\mu$	=	dynamic viscosity, $Pa \cdot s$
$\omega$	=	vorticity, $s^{-1}$
$\Omega$	=	angular rotational speed of fan, $rad/s$
$\tau_{ij}$	=	viscous stress tensor, $N/m^2$
$\rho$	=	density
$\delta$	=	boundary layer thickness, $m$
$\delta_v$	=	viscous wall scale, $\mu/(\rho u_\tau)$ , $m$
superscript	=	
+	=	wall unit, normalised using the viscous wall scale $\delta_v$
'	=	fluctuation about the time mean
superscript	=	
<i>abs</i>	=	absolute frame of reference
<i>rel</i>	=	relative frame of reference, attached to the rotational fan
<i>inl</i>	=	inlet

## I. Introduction

As the bypass ratio increases to pursue higher engine efficiencies, the fan becomes a key contributor to thrust and also noise. When an aircraft is landing, the fan is running at a lower speed, leading to excessive separation in the tip region. Even within the stable operation range, this separation will also lead to significant aerodynamic loss and noise emission. The noise is composed of tonal and broadband components. The tonal noise has been fairly well reduced by frequency-tuned acoustic liners, which makes the broadband component stand out. Broadband noise is closely related to the turbulence generated in the fan separations and wakes. This emphasises the importance of accurate prediction of fan turbulence. On the other hand, the engine is now made increasingly compact to reduce weight and aerodynamic drag. This results in stronger interaction between adjacent components. In a fan configuration, fan blades are neighboured by a bypass splitter ring as well as bypass and core duct stators. The downstream effects are not negligible on the development of fan separation and wake. The complexity of both turbulence and geometry in this fan stage, sketched in Fig. 1, make the simulation of this closely coupled fluid system extremely challenging. This type of simulation has also been listed as one of the grand challenges in the NASA CFD Vision 2030 [1]. The challenge mainly comes from two aspects. First, the separation and wakes need to be predicted by high-fidelity simulations, such as Direct Numerical Simulation (DNS) and Large-Eddy Simulation (LES), but they are prohibitively expensive to be used for the whole fan stage. Second, the modelling and meshing process of complex geometries is difficult and time-consuming, considered as the main barriers to CFD autonomy, especially for bypass fan configurations with stationary and rotating components.

Even if the mesh could be automatically generated, the generation process for such large-scale high-fidelity simulations still faces other issues with the effective utilization of high-performance computing [2]. One feasible solution to these could be: treat flow and geometry by zones with various modelling fidelities according to the local accuracy requirement. It could provide an accurate prediction of sophisticated turbulent flow features at a minimal computational effort. This forms the aims of this research.

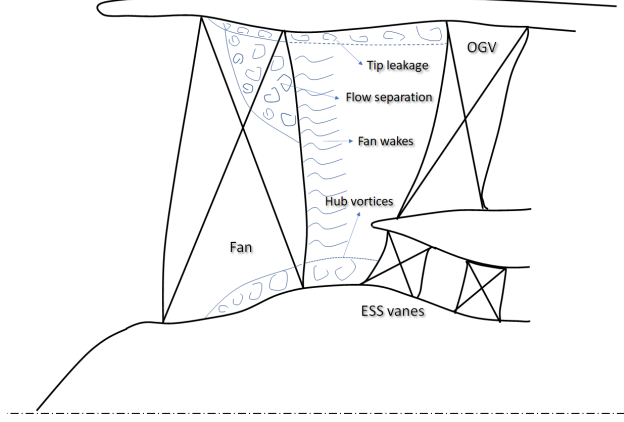


**Fig. 1 Flow topology at the approach condition**

Integrating different fidelity levels of turbulence and geometry modelling in one simulation allows an increase in computational speed. This enables the simulation of large-scale aerodynamically coupled systems at a minimum cost to meet the required accuracy. Conventionally, the degree of modelling in a simulation is described as the fidelity levels of a solution, and the fidelity decreases with modelled content. However, it is necessary to distinguish fidelity from accuracy. A low fidelity model, operating in the calibrated space, is able to reproduce results as well as a higher fidelity simulation. Rather, an increase in fidelity provides more flow detail and requires less empiricism. The coupled fluid problem can be solved by integrating models of different fidelities in one solution: flow zones with adequate knowledge solved by well-calibrated low-fidelity models while zones with little knowledge solved by high-fidelity eddy-resolving and fully geometry resolved methods. The consistent accuracy could be achieved in one solution with sufficient flow detail provided in the region of interest.

Turbulence and geometry modelling can be pursued in a coherent framework, as there is a hierarchy of methods from low to high fidelity levels with the structural similarities shared in the governing equations, shown in Fig. 2. With the increase of simulation fidelity, the modelled content decreases while the resolved content and simulation cost increase. For turbulence modelling, the hierarchy is built on how much of the turbulent scales are modelled. At the low fidelity end, Reynolds Averaged Navier-Stokes (RANS) equations are solved to model all turbulent scales, while at the high-fidelity end, the Navier-stokes equations are directly solved in DNS to resolve all the scales without modelling. LES trades off between the ends, resolving only the large-scale turbulent motion with grid cut-off scales modelled. A similar

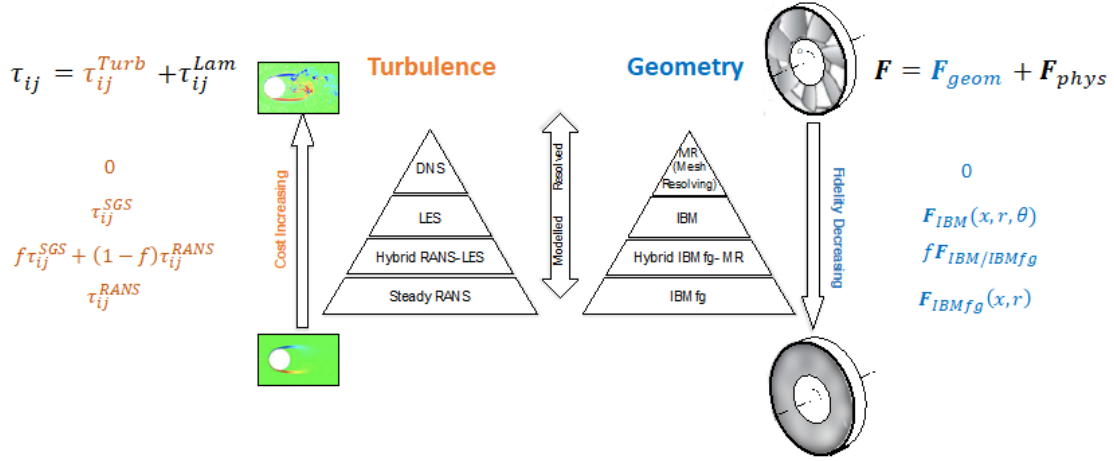


**Fig. 2 Hierarchy of turbulence and geometry modelling, adapted from [12]**

hierarchy exists in geometry modelling, which is less recognised than that of turbulence. This geometry modelling hierarchy depends on how much the geometry is explicitly resolved. The most common way is to resolve the full geometry using body-conformal mesh, which is at the top fidelity level. As mentioned before, this can be challenging for complex geometries and moving bodies. Going down the hierarchy, a body force is introduced to model the geometry instead of resolving on grids. Immersed Boundary Methods (IBM) were developed to represent the geometry on the Cartesian mesh using the distribution of body forces [3]. This has greatly offloaded the mesh generation task with a wide use for fluid-structure interactions. For the internal turbomachinery flows, the IBM could be further simplified by filtering out the blade geometry with azimuthal homogenous distributed blade forcing terms [4]. This is referred to as IBMfg – IBM with filtered geometry (fg) - in this paper. As only the radial profile of azimuthally-averaged flow is captured in IBMfg, it is placed at the low-fidelity end. For both geometry and turbulence modelling, the hybridization could be made across the hierarchy to zonalise the high-fidelity method in the region where it is needed most. Several attempts have been successful from either turbulence or geometry modelling aspects. Some typical examples for hybrid turbulence modelling are Detached Eddy Simulation (DES) [5], Zonal DES (ZDES) [6] and Embedded LES [7, 8], while the hierarchical geometry modelling can also be found in a few cases [9–11].

In this research, a demonstration has been made by combining hierarchical modelling of both geometry and turbulence in one simulation of fan stage flows. This is achieved by zonalising LES in the fan tip region for separated flows and lower-order modelling the downstream stators with IBMfg. The paper is organized as follows: the strategy of hierarchical turbulence and geometry modelling is firstly explained in detail and its implementation is provided for the fan stage. The hierarchical method is then fully validated by comparing the prediction with experimental measurements and the sensitivity of the RANS-LES interface is investigated. To illustrate the benefits of using hierarchical modelling, the cost and accuracy has been discussed in comparison with other existing simulation methods. Finally, the simulation

results are used to assess the isotropic turbulence assumption in the low-order acoustics model.

## II. Methodology

### A. Governing equations of hierarchical turbulence and geometry modelling

The structural similarities in the governing equations provide the theoretical foundation for a hierarchy of turbulence and geometry models. The governing equations are given in a general integral form, discretised by finite volume method:

$$\frac{\partial}{\partial t} \int_{\Omega} \mathbf{Q} dt + \oint_{\Gamma} \mathbf{G}_i n_i dA = \int_{\Omega} \mathbf{F} dV \quad (1)$$

where  $\Omega$  and  $\Gamma$  are control volume and surfaces of a mesh cell in the computational domain, and  $n_i$  is the  $x_i$  component of a unit surface normal vector pointing outwards.  $\mathbf{F}$  represents volumetric source/force, which contains both physical sources  $\mathbf{F}_{phys}$  and geometrical forcing  $\mathbf{F}_{geom}$ . The physical source  $\mathbf{F}_{phys}$  refers to the volumetric sources induced by any physical processes, such as volumetric heat, buoyance, gravity, Coriolis and centrifugal forces. The geometry force refers to the force exerted on fluid particles from the geometry boundaries and will be discussed later in detail. The conservative variables  $\mathbf{Q}$ , convective and viscous flux  $\mathbf{G}_i$  are written as

$$\mathbf{Q} = \begin{bmatrix} \rho \\ \rho u_1 \\ \rho u_2 \\ \rho u_3 \\ \rho E \end{bmatrix}, \mathbf{G}_i = \begin{bmatrix} \rho u_i \\ \rho u_1 u_i + p \delta_{i1} - \tau_{i1} \\ \rho u_2 u_i + p \delta_{i2} - \tau_{i2} \\ \rho u_3 u_i + p \delta_{i3} - \tau_{i3} \\ \rho H u_i - \tau_{ij} u_j + q_i \end{bmatrix} \quad (2)$$

The definition of viscous stress tensor  $\tau_{ij}$  and source term  $\mathbf{F}$  leads to a hierarchy of turbulence and geometry models.

For turbulence modelling, there are structural similarities shared by the RANS, LES and DNS equations. Although the primitive variables solved in the equations are ensemble-averaged in RANS and spatially filtered in LES, the key difference lies at the modelled turbulent stress tensor  $\tau_{ij}$  within the total viscous stress tensor

$$\tau_{ij} = \tau_{ij}^{lam} + \tau_{ij}^{turb} \quad (3)$$

where  $\tau_{ij}^{lam}$  is the physical viscous tensor. In DNS, the modelled turbulent stress  $\tau_{ij}^{turb}$  is zero as all the turbulent scales are directly resolved on grids. This modelled term appears in LES and RANS, and can be framed in a general form:

$$\tau_{ij}^{turb} = (1 - f) \tau_{ij}^{RANS} + f \tau_{ij}^{LES} \quad (4)$$

where  $\tau_{ij}^{RANS}$  is the Reynolds stress tensor provided by RANS modelling and  $\tau_{ij}^{LES}$  is the subgrid stress tensor modelled in LES to account for unresolved turbulence scales. If  $f$  is a global parameter, the simulation will run in pure LES ( $f = 1$ ) or pure RANS ( $f = 0$ ) mode. If  $f(\mathbf{x})$  is a spatial blending function between 0 and 1, it defines the strategies of hybrid LES-RANS. This stress blending formulation (4) is able to incorporate the concept of wall-modelled LES, zonal/embedded LES and DES-type of methods. It is also worth noting that the  $\tau_{ij}^{RANS}$  and  $\tau_{ij}^{LES}$  can be provided independently using different RANS models and LES subgrid models. In the current simulation, the LES stress is provided by the Wall-Adapting Local Eddy-Viscosity (WALE) subgrid model [13] and the RANS stress is provided by the one-equation Spalart-Allmaras model [14].

For geometry modelling, the hierarchy is reflected in the definition of geometry forcing  $\mathbf{F}_{geom}$ , as shown in Fig. 2. When  $\mathbf{F}_{geom} = 0$ , the simulation is performed with direct mesh-resolved geometries. In the IBM, non-zero localised  $\mathbf{F}_{geom}$  is introduced to model the force exerted on fluids by solid boundaries instead of resolving the real geometry by body-conformal mesh. The fidelity level in the IBM category depends on how accurate  $\mathbf{F}_{geom}$  describes the geometry. In the normal IBM,  $\mathbf{F}_{geom}$  is a function of three-dimensional coordinates  $\mathbf{x} = (x, r, \theta)$  that exactly enforces the effect of discrete real geometry boundaries. Moving to lower fidelity levels, more geometry features become filtered and will be modelled. In the IBMfg, which is used in this research, the blade/stator geometry is circumferentially filtered out with its azimuthal mean effect modelled by the two-dimensional body force

$$\mathbf{F}_{geom} = \begin{bmatrix} 0 \\ f_{b,1} + \frac{1}{\lambda} P \frac{\partial \lambda}{\partial x_1} \\ f_{b,2} + \frac{1}{\lambda} P \frac{\partial \lambda}{\partial x_2} \\ f_{b,3} + \frac{1}{\lambda} P \frac{\partial \lambda}{\partial x_3} \\ f_{b,i} u_i \end{bmatrix} \quad (5)$$

where  $f_{b,i}$  is the blade force acting on the fluid in the direction  $x_i$ , and  $\lambda$  is the factor that accounts for the blade thickness blockage. The body force term  $f_{b,i}$  and blockage factor  $\lambda$  are only active in the blade/stator region.

The blade forcing term  $f_{b,i}$  consists of two parts

$$f_{b,i} = f_{bn,i} + f_{bp,i} \quad (6)$$

where  $f_{bn,i}$  is the normal blade force that imposes non-permeable boundary and guides the flow turning along the blade camber line. This is implemented using the proportional integral (PI) controller which drives the computed velocity  $u_i^n$  to the desired velocity  $u_i^D$  at the smeared blade region.

$$f_{bn,i} = K_p(u_i^D - u_i^n) + K_I \int_0^{t_n} (u_i^D - u_i^n) dt \quad (7)$$

In the above,  $K_p$  is the coefficient of proportional controllers with dimension of  $s^{-1}$  and controls the convergence speed to the desired value as a damping factor.  $K_I$  is the coefficient of the integral controller with dimension  $s^{-2}$  and is used to increase computational stability.  $f_{bn,i}$  will vanish when the computed velocity is parallel to the blade camber line.  $f_{bp,i}$  is the parallel blade force that is calibrated to model the blade profile and endwall loss. This IBMfg has been well validated and was used to study the mutual interactions between intake-distortion and fan in our previous research [15, 16].

## B. Hierarchical modelling strategy for fan stage flows

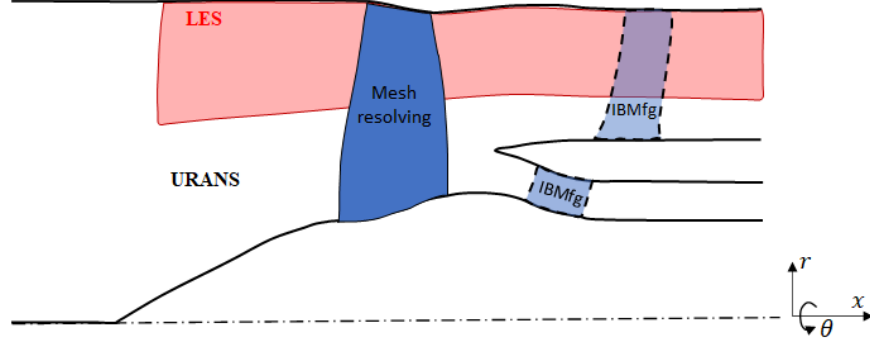
Figure 3 shows the simulation strategy of a fan stage with bypass duct configuration. The fan is running at half of the design speed, the mismatch between flow and blade angle causes excessive separation in the tip region. Hence, the LES is zonalised in the fan tip to capture complex tip flows, including separation on the blade and near the endwall as well as leakage from the tip gap. Compared to the tip flows, the flow in the lower span is relatively clean without too much separation. Hence, RANS is used in this region to save computational cost. The interface between RANS and LES is placed at approximately 50% span in the fan region and follows a streamline in the meridional plane. As our research is focused on the fan flow, the downstream stators, including OGV in the bypass and ESS in the core, are modelled in a low-order way using IBMfg, which predicts the azimuthally averaged behaviour of the stators. This provides the fan with a suitable outlet condition from downstream stators and creates potential field interactions with the upstream fan but without substantial increase of computational cost. Even if the OGV potential field effect can be neglected and a radial static pressure profile could be used at the outlet boundary, the simulation still requires a strict non-reflective outlet boundary condition to prevent the reflection from the impingement of unsteady fan wake on the outlet, as the outlet is too close to the fan blade and this leaves no more space for a sponge region. In comparison, our IBMfg still provides a better solution which enables a sponge region downstream of the OGVs and further reduce any possible numerical reflections.

Figure 4 shows the implementation of hybrid LES-RANS modelling based on the turbulence stress blending formula given by Eq. 4. The lower half span is set in the RANS mode with  $f = 0$ , while the upper half span is specified with  $f$  defined by the Eq. 8 to zonalise LES in the fan tip region with a thin RANS layer from the 50% span location.

$$f(d_w) = \min[\max(\frac{d_w - (1 - \beta)d_{RANS}}{\beta d_{RANS}}, 0), 1] \quad (8)$$

where  $d_w$  represents the wall distance, and  $d_{RANS}$  represents the RANS layer thickness;  $\beta$  defines the size of RANS-to-LES transition zone. In the LES zone, the thin RANS layer of  $y^+ \sim 100$  is placed near the fan blade and casing





**Fig. 3 Schematics of hierarchical modelling strategy of a fan stage**

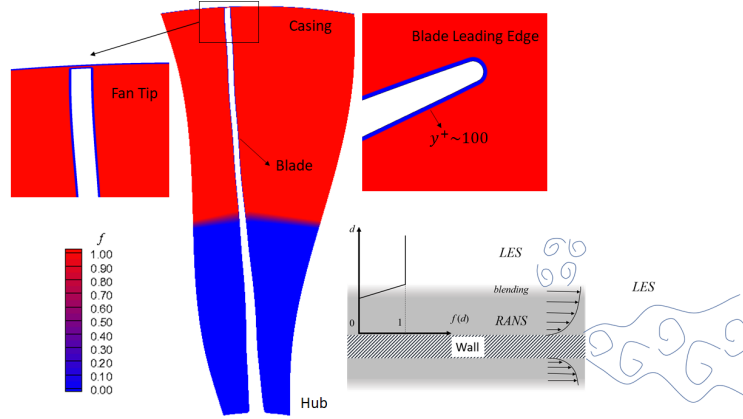


**Fig. 4 Blending function distribution of zonalised LES in the fan passage**

as a wall model. This avoids the cost of resolving near-wall turbulent streaks. Attached boundary layer exists on the blade pressure surface. To illustrate the effectiveness of the wall modelling, the boundary layer velocity profile near the trailing edge on the pressure surface is plotted with the wall units in Fig. 5. The velocity profile in the boundary layer is well produced by this simulation. The LES-RANS interface sits in the log region with limited effects on the velocity profile as the rapid switch from RANS to LES is achieved using the defined blending function  $f$ .

Figure 6a demonstrates the role of IBMfg OGV modelling. Compared with the flow field of the single rotor simulation in Fig. 6b, the IBMfg body force is imposed azimuthally uniform in the OGV region without the geometry meshed but turns the flow following the OGV camberline as it should have when the OGVs were present. The velocity relative to the rotational frame is plotted so the tangential velocity increases in the negative  $t$  direction because of the OGV cambering. If sitting in the absolute frame, the radial distribution of tangential velocity is shown in Fig. 6c. The IBMfg result is compared with those of single rotor and mixing-plane stage calculations. The incoming flow before the fan is in the axial or  $x$  direction without the tangential component. The fan blade inputs work to the fluid by adding swirls as indicated in the single rotor results. The OGVs take swirls out to achieve the pressure rise. After the OGVs, the tangential velocity becomes around zero. The IBMfg fulfills this task and shows a agreement with the mixing-plane

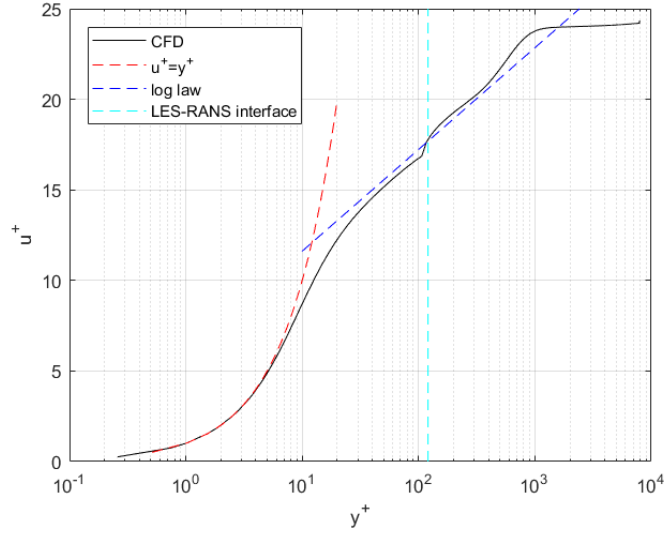
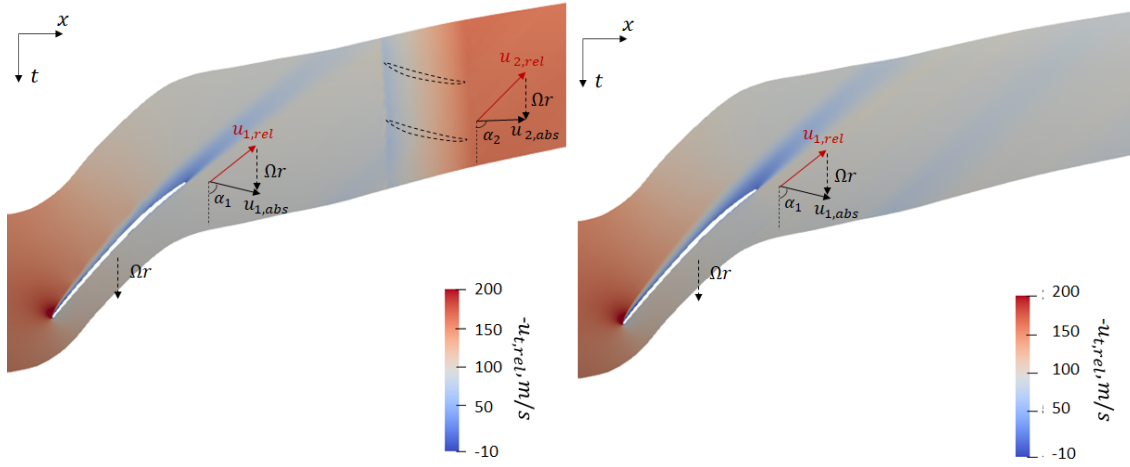


**Fig. 5** Boundary layer profile on the pressure surface near the trailing edge of the fan blade, where  $Re_\theta = 4160$

stage simulation. This is also reflected in the absolute flow angle shown in Fig. 6d. The IBMsg achieves the target by turning the flow back to the axial direction. Since endwall models have not been implemented in IBMfg to account for secondary flows, so the discrepancies are expected between the IBMfg and the stage simulation in the endwall region. However, this doesn't significantly affect the overall accuracy of the simulation and can be improved in the future.

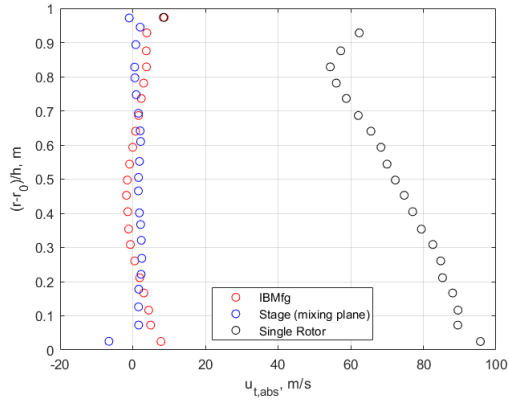
The hierarchical modelling strategy mentioned above was implemented in an unstructured edge-based solver for compressible flows. The kinetic energy preserving scheme [17] is used to keep the numerics at a low dissipation level that is suitable for LES. The time advancement is achieved using the 2nd order backward Euler difference with dual time stepping. The simulation is performed in the rotational framework with absolute boundary conditions set at the inlet and outlets. The total temperature and pressure are imposed at the inlet and static pressure with radial equilibrium conditions are set at both bypass and core duct outlets.

For the simulation mesh, hexahedral cells are used here to improve mesh quality although the flow solver was written for computation on unstructured meshes. The fan blade is mesh-resolved while downstream stators are modelled by IBMfg without geometry conformal mesh blocks. The mesh around the fan blade is illustrated in Fig. 7. An O-grid is employed to provide high-quality orthogonal mesh to the boundary layers on blade and endwall surfaces. The grid spacings are listed in Table 1. Grid points are clustered around blade leading and trailing edges and gradually expanded into the mid-chord with maximum streamwise grid size  $\Delta s^+ = 600$  in terms of wall units. The first cell wall distance  $\Delta d_w^+$  on the blade and endwalls are between 0.5 and 3. The maximum spanwise grid size  $\Delta r^+$  in LES zone is around 300. These all satisfy the grid density requirement of hybrid RANS-LES [18]. This leads to 63 million cells in total. The time step is  $1.2 \times 10^{-3} c/u_{inl}$ , where  $u_{inl}$  is the freestream velocity at the inlet. The simulation has run over  $64.3c/u_{inl}$  to obtain the flow statistics.

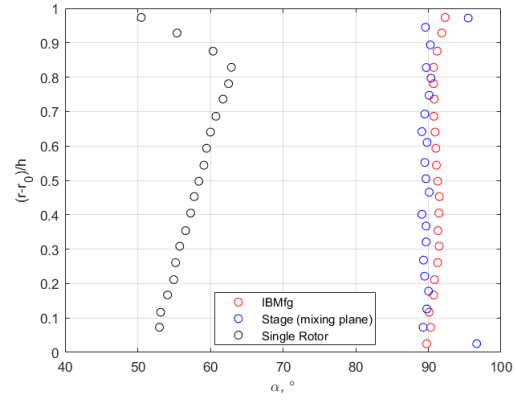


(a) relative tangential velocity with IBMfg

(b) relative tangential velocity without IBMfg

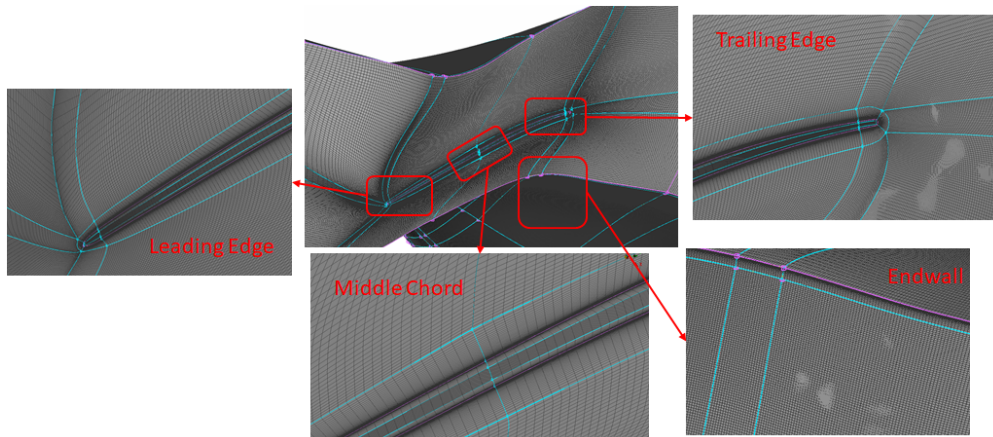


(c) absolute tangential velocity downstream OGVs



(d) absolute flow angle downstream OGVs

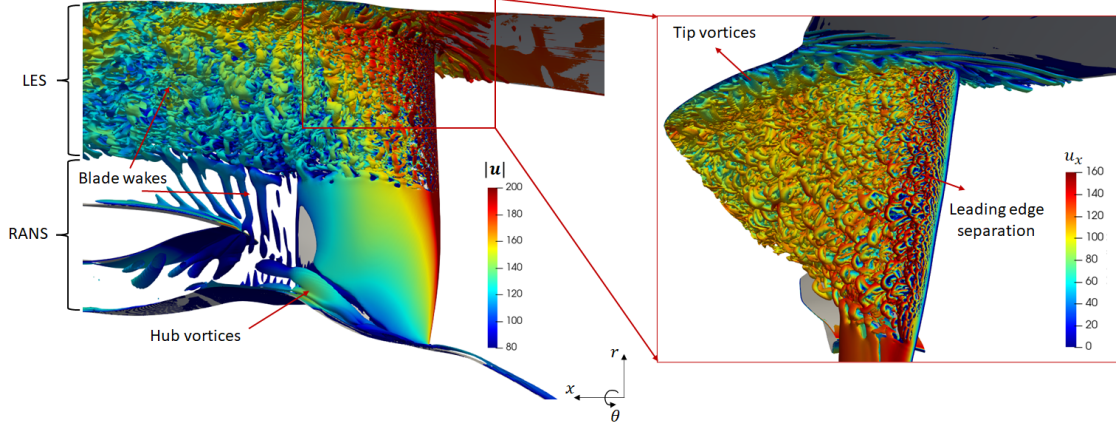
**Fig. 6** Flow field of IBMfg modelling of OGVs compared with those of single rotor and mixing-plane stage simulation



**Fig. 7** Mesh distribution in the fan region

**Table 1 Streamwise grid size distribution along fan blade surface**

Locations	Leading Edge	20% $c$	50% $c$	80% $c$	Trailing Edge
$\Delta s^+$	10	100	600	150	15

**Fig. 8 Q-criterion isosurfaces illustrating flow structures captured by zonalised LES in the fan tip region**

### III. Results and Discussions

#### A. Instantaneous flow field

Zonalised LES has been performed in the upper span of the fan passage. Figure 8 shows the flow structures from this simulation. The flow structures are visualised by Q-criterion isosurfaces. Fine-scale turbulence has been well resolved by LES from the fan tip to the middle span while ensemble-averaged large-scale wake structures and horse-shoe hub vortices are captured by RANS. A close-up view of the tip region shows the structures resolved by LES. The hairpin vortices roll up near the leading edge and flow separations occur on the fan blade in the upper span. This is due to the positive flow incidence at this off-design rotational speed which is half of the design speed. In the tip region, the incoming boundary layer at the casing stagnated around the fan blade leading edge and generates horse-shoe vortices in the tip corner. The tip leakage flows are weak compared to the horseshoe vortices because the tip clearance is relatively small, which is 0.28 percent of span length.

Figure 9 shows the ratio of turbulence modelling and physical/laminar viscosity and the vorticity magnitude at an axial plane located around 33 percent fan chord  $c$  downstream of the fan. The majority of turbulent energy is directly resolved on grids by LES rather than modelled by the turbulent stress  $\tau_{ij}^{turb}$ . This is opposite in RANS, where most of the turbulent energy is modelled. Hence, the turbulence modelling viscosity is high in the wake of the lower-span RANS region and fades away towards the fan tip in the upper-span LES region. This modelling difference is also reflected in the vorticity. LES is zonalised in the upper span, resolving fine-scale turbulent structures in the wake and endwall regions. The flow field makes a smooth transition into the reduced flow-scale RANS region in the lower span. This indicates that the LES has been successfully blended into the RANS context.

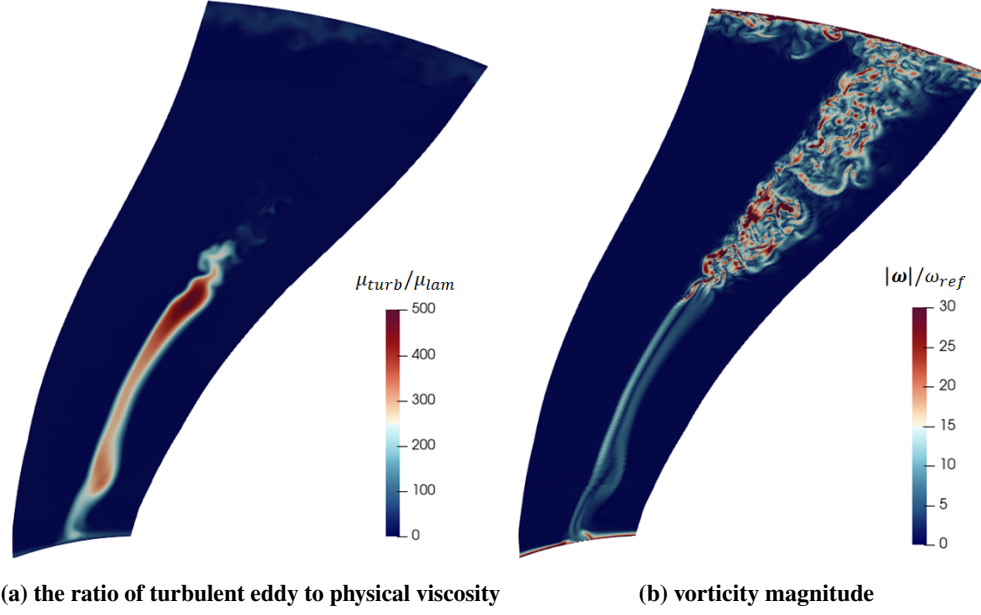


**Fig. 9** RANS eddy viscosity and vorticity magnitude in an axial plane that is 33%  $c$  downstream of the fan blade

### B. Time-averaged flow fields

The time-averaged flow fields from the simulation are compared with the experimental measurement at the same plane downstream of the fan. The experimental measurements were performed using hot wires at an interstage position with a fixed azimuthal location and 33 radial transverse positions [19]. The averaged flow fields from experimental measurements are obtained by phase averaging. Fig. 10 shows the comparison of axial velocity between simulation and experiment. Passage-to-passage variations are present in the experiment. This could be caused by manufacture and installation variations of the fan blades as well as mechanical vibration during the operation. In the simulation, only one blade passage is computed and repeated 20 times to form the whole annulus. The same contour levels are used for this comparison. The LES captures the fan suction surface separation and the wake shape shows a qualitative agreement with that of the experiment in the upper span. RANS is smoothly blended with LES and yields a reasonable prediction of the low-span flow.

Figure 11 compares the turbulent fluctuations of axial velocity from both experiment and simulation. In the simulation, the turbulent fluctuations are hardly seen in the lower span, because they are intrinsically modelled in RANS instead of resolved on grids in LES that is used in the upper span. The comparison between simulation and measurement on the turbulent fluctuations are therefore focused at the upper span. Although the experiments show large passage-to-passage variations, the LES generally captures the shape of high fluctuations regions. The predicted fluctuation level is in a reasonable range compared to that of experiment. In the tip, the high fluctuation and low-velocity region is caused by tip leakage flows and casing horseshoe vortices. This is slightly under-predicted by the simulation. A possible reason is that the tip clearance is larger in the experiment than the designed value used in the simulation.

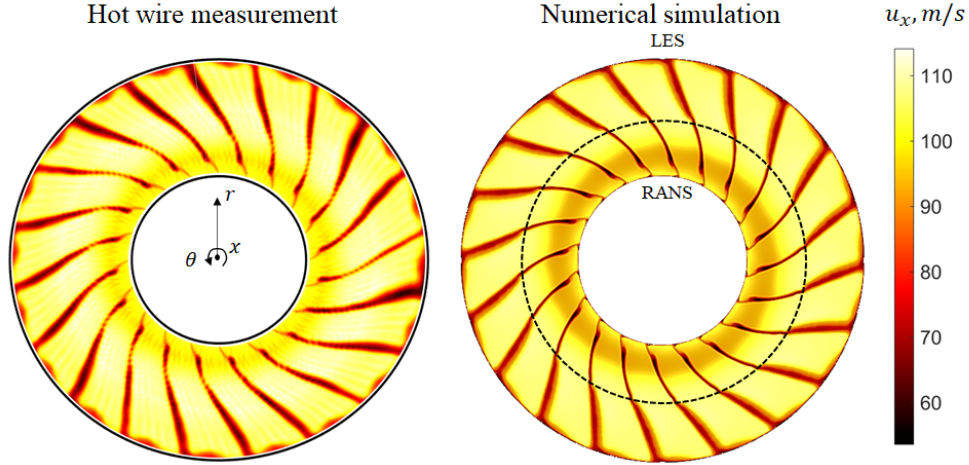


**Fig. 10** Axial velocity from hot-wire measurements and numerical simulation downstream of the rotor

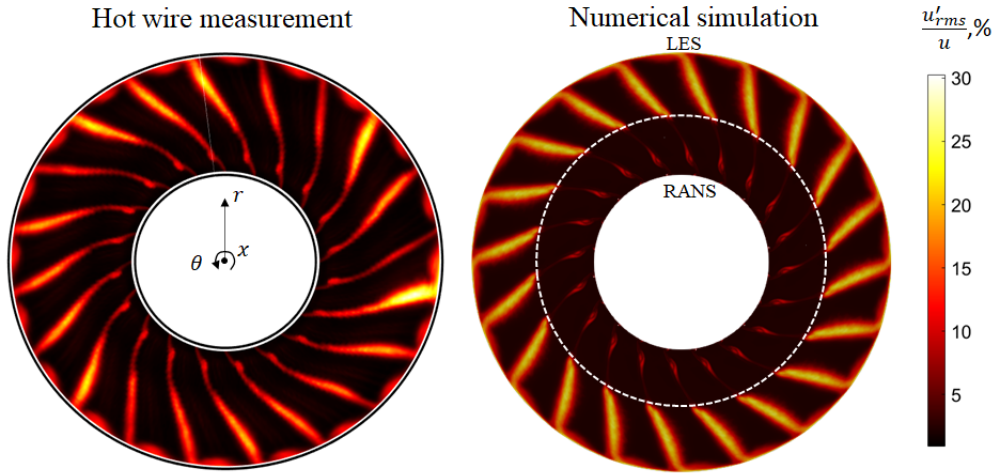


**Fig. 11** Turbulent fluctuations of axial velocity from hot-wire measurements and numerical simulation downstream of the rotor

Overall, a qualitative agreement has been achieved between simulation and experiment.

### C. Wake profiles

The wake profiles are quantitatively compared with the experimental measurements at various radial locations. Figure 12 shows the azimuthal velocity profiles across the wake in the upper-span LES region. Four radial locations, *i.e.* 90%, 80%, 70% and 60% of the span, are selected for this comparison. The measured wake profile from a reference passage is plotted as a solid line. The variations across passages are represented by shaded areas. The LES prediction of axial velocities, plotted by red circles, shows an excellent agreement with the reference passage measurement in terms of the wake depth and width. The blade wake reaches a maximum width near 70% span because of the separation on the suction surface. LES predictions of radial and tangential velocities also show a reasonable agreement with the

measurements, although consistent overprediction is observed. This overprediction is also present in the eddy-resolving predictions of the other partners in the same EU project using wall modelled LES [20] and ZDES [21]. This indicates a possibility of hot-wire measurement uncertainty. However, the overall shape and location of the wake is well captured and most of the predictions lie close to the range of passage-to-passage variation.

In addition to mean velocity profile, the azimuthal variation of velocity fluctuation intensity is shown in Fig. 13. The velocity fluctuations are provided in three directions, i.e. radial, axial and tangential. The intensity of velocity fluctuations in each direction is obtained by normalising the root square mean (rms) of fluctuations by the time-averaged total velocity. They are plotted at the same span locations as the velocity profiles. The LES generally agrees with the measurements and lies within the passage variations. There are two peaks in the profiles at the 90% span. The first peak is caused by the tip vortices. This is slightly underpredicted by LES as the tip clearance in the simulation might be different from that in the experiment. The first peak disappears at lower span locations while the second peak remains. The second peak, corresponding to the blade wake, is reasonably predicted by LES. Within the passage-to-passage variation, the prediction is generally higher than that in the reference passage. This could be related to the frequency cut-off in the measurement because of the wire size. This potentially leads to a low measured turbulent intensity [22] and this overprediction is also consistent with that of the wall modelled LES [20] and ZDES [21] of our project partners. The overall agreement between simulation and experiment is satisfactory taking all these factors into account.

In the lower-span region, where the simulation is switched to RANS mode, the predicted axial velocity profiles are plotted against the experimental measurements in Fig. 14. Since the one equation SA model is used for RANS modelling, the axial velocity turbulent fluctuation is not available to directly compare with the measurements. However, the wake velocity profiles predicted by RANS agree reasonably well with the measurements, as flows are attached to the blade in most of the lower span region. The wake shape and location are well captured, but with a thinner and deeper wake predicted. This is a well-known deficit of RANS models. The results indicate that RANS has been successfully integrated with LES and is able to generate reasonably accurate results in a less separated flow region.

#### **D. Effects of RANS-LES interface**

In the current simulation, the RANS-LES interface has been placed at 50% span following a streamline. There might be some concerns that the interface could add some degree of resistance to the resolved turbulent fluctuations in the upper-span LES and the RANS-LES interface could be sensitive to the radial location. To test these, another simulation has been made by moving the interface from the 50% to 40% span. The axial velocity and its fluctuations are plotted in Fig. 15 directly at the radial locations of the LES-RANS interfaces of the two simulations, *i.e.* 50% and 40% span, and compared with the measurements. At the 50% span location shown in the Fig. 15a, the interface shows negligible effects on the velocity prediction. The axial velocity is well predicted by the simulation with the LES-RANS interface at the same span location (50% span) compared with the experimental data and lies close to the other simulation result



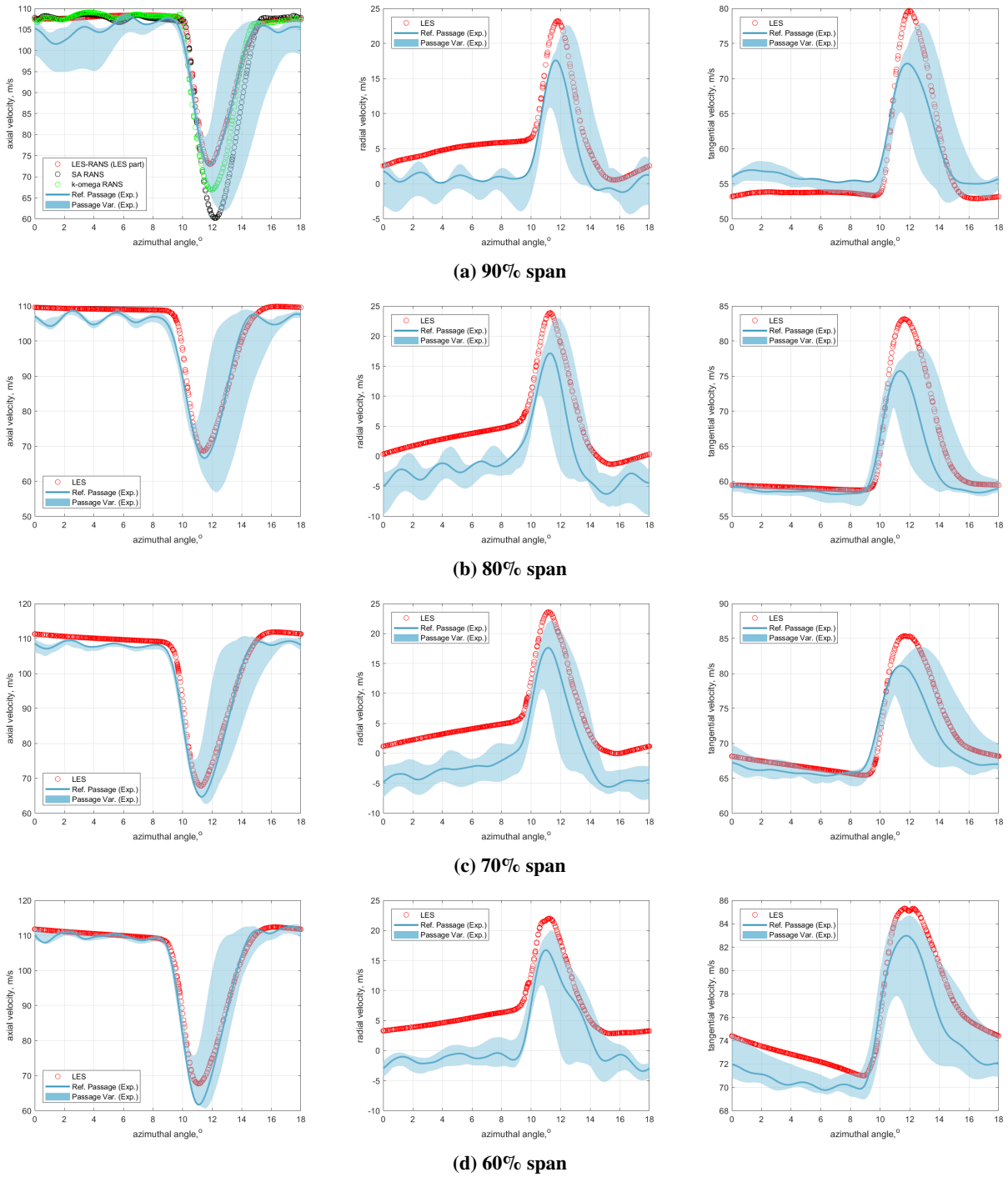


**Fig. 12** Azimuthal velocity wake profiles at the 90%, 80%, 70% and 60% span locations in the interstage measurement plane downstream of the fan rotor



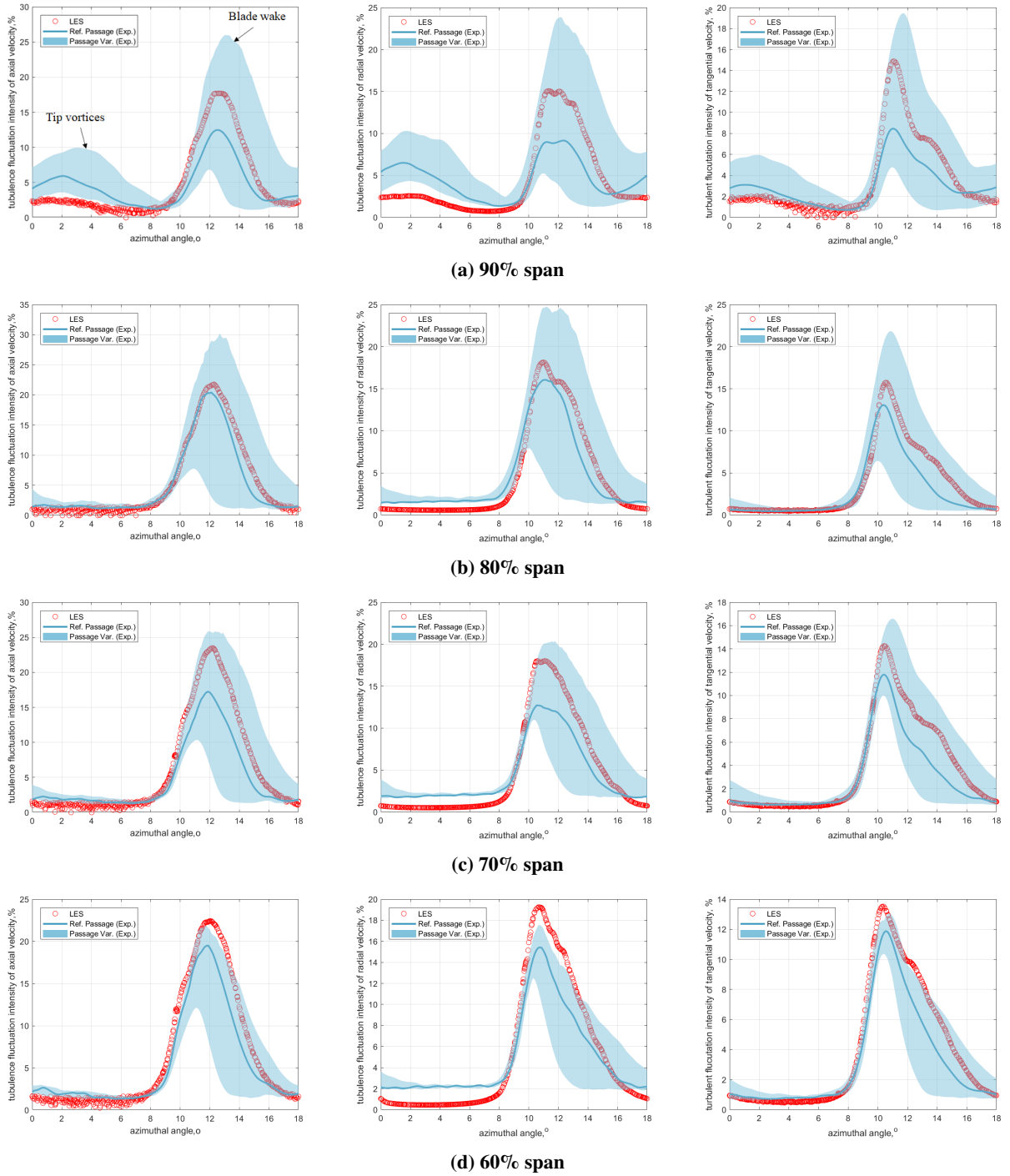


**Fig. 13** Azimuthal wake profiles of velocity fluctuations at the 90%, 80%, 70% and 60% span locations in the interstage measurement plane downstream of the fan rotor

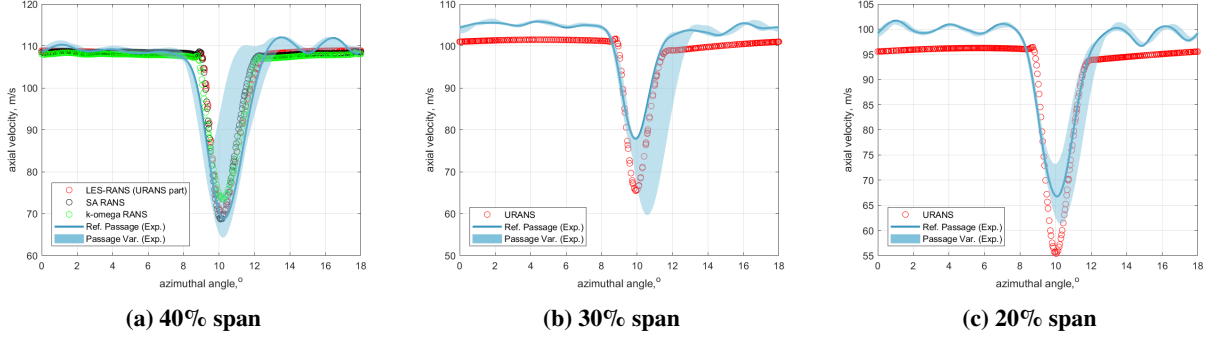
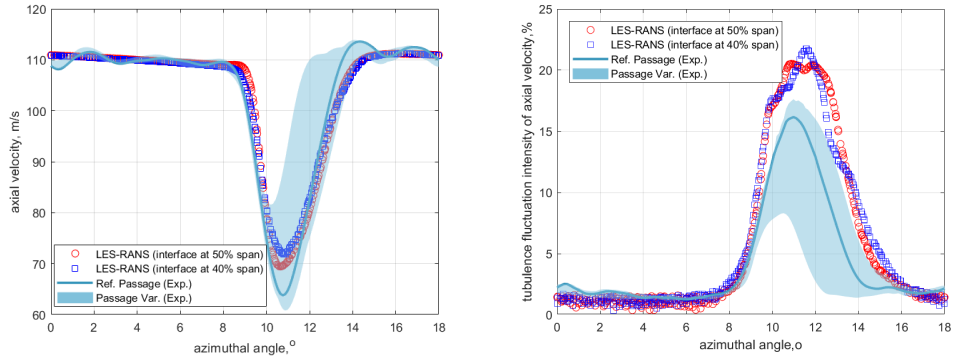


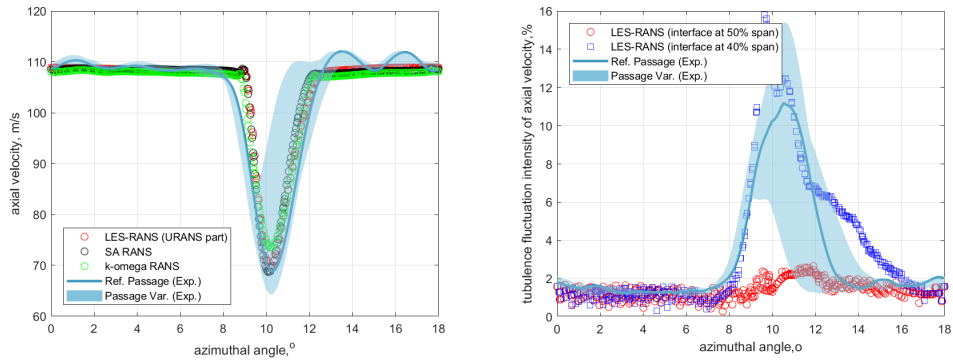
**Fig. 14 Azimuthal profile of axial velocity at 40%, 30% and 20% span locations in the interstage measurement plane downstream of the fan rotor**

with the interface at the 40% span. The turbulent fluctuations are slightly overpredicted in the wake, but the shape and location have been captured and consistency is observed between the two simulations with different radial locations of LES-RANS interface. The comparison of the two simulations indicates that the presumed interface-added resistance to resolved turbulence at 50% span is very limited. This suggests that the flow prediction at the interface is not significantly affected by the switch of simulation modes between LES and RANS. This point is also verified by the results at the 40% span location. Figure 15b shows that the predicted velocity profiles of the two simulations align close to each other and agree fairly well with the reference passage and within the passage-to-passage variation. The turbulent fluctuations are also reasonably predicted by the simulation with 40% span interface. For the simulation with 50% span interface, the 40% span location is in the RANS region where the turbulent fluctuations are not resolved, hence the predicted turbulent fluctuations are at a low level. Generally, reasonable agreement has been achieved with experimental measurement at the LES-RANS interface and shows that the interface has limited effects on the prediction.

To check if the radial position of LES-RANS interface will affect the prediction at other span locations, the azimuthally averaged velocity profiles of the two simulations are plotted in Fig. 16. The experimental measurements are averaged over the whole annular and plotted as solid lines with the passage variation denoted. The LES-RANS interfaces are marked by dashed lines with the same colour as the simulations. The predicted three velocity components from the two simulations show little difference across the whole span. This shows that the entire simulation prediction is not sensitive to the LES-RANS interface location. The predicted axial and tangential velocity profiles agree reasonably well with the experimental data. The predicted radial velocity captures the shape of experimental data but is offset. This is the same as discussed before that the absolute amplitude of radial velocity is too small to measure with enough accuracy using hot wires. This result is also consistent with the other predictions made by WMLES [20] and ZDES [21]. Close-up plots are made in Fig. 17 at the two span locations, *i.e.* 60% and 30% span, relatively close to the LES-RANS interfaces but located in the LES and RANS regions respectively. The two simulations coincide with each other. This further confirms that the radial RANS-LES interface doesn't affect the simulation results and the proposed zonalised



(a) 50% span



(b) 40% span

**Fig. 15** Azimuthal profiles of axial velocity and its fluctuations at the RANS-LES interfaces of the two simulations, *i.e.* 50% and 40% span

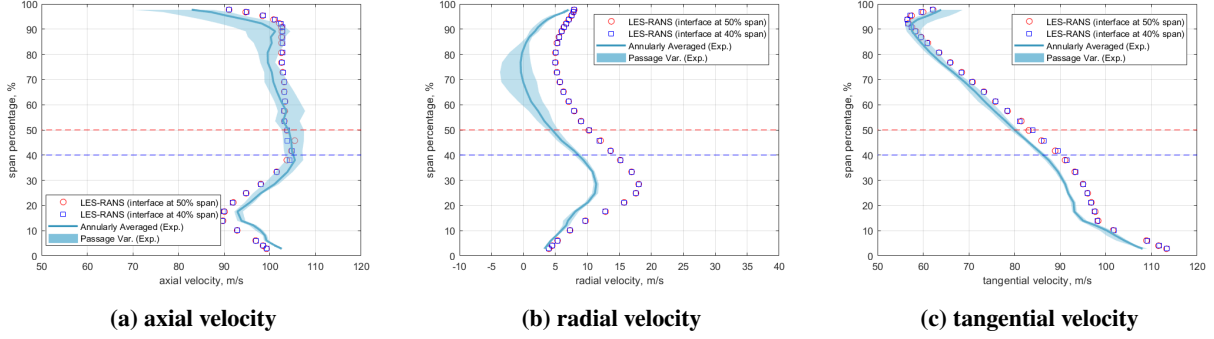


**Fig. 16** Radial profiles of azimuthally averaged velocity for the two simulations with the LES-RANS interface at 40% and 50% span locations

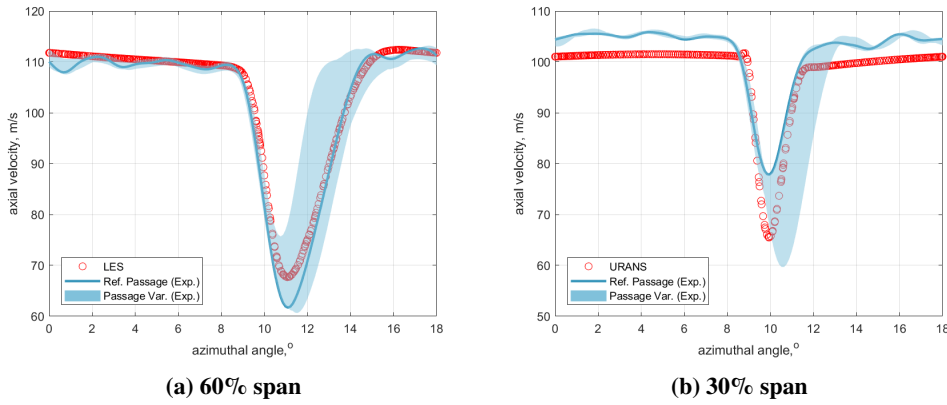


**Fig. 17** Comparison of azimuthal profiles of axial velocity and its fluctuations of the two simulations at the 60% and 30% span, representing the results in the LES and RANS regions respectively

LES strategy is robust.

## E. Discussion on accuracy and cost of hierarchical modelling

The hierarchical modelling trades off between cost and accuracy by treating the simulation zonally with different levels of fidelities. The benefits of this zonal method can be seen from the absolute accuracy and relative cost. The absolute accuracy has already been confirmed by comparing the predicted wake profiles with experimental measurement in the section III.C. To further illustrate this point, the results are compared with two RANS models, Spalart-Allmaras [14] and  $k - \omega$  SST model [23], in Fig. 18 at two representative span locations: one at the 90% span where separation and leakage are present, and the other at the 40% span where flows are attached to fan blade. In the separation region, shown in Fig. 18a, the zonalised LES shows a clear advantage over the RANS models in term of accuracy. Axial velocity shows that both of the RANS models predict larger separation on the fan blade, leading to a wider and deeper wakes. Since the separation is overpredicted, the flow turning is underpredicted by the RANS models. The comparison of turbulence intensity at 90% span location also shows that the RANS model is incapable of capturing the position of

tip vortices (the first peak) and overpredicts the turbulence inside the wake (the second peak). In contrast, our zonalised LES method predicts all these quantities well and agrees with experimental data. In addition, the lateral comparison has also been made between our prediction and other high-fidelity methods from our project partners, *i.e.* full-span wall-modelled LES (WMLES) [20] and ZDES methods [21]. Similar level of accuracy has been found across the three types of simulations, and the results are published in a project deliverable report [24]. At the 40% span location, where flows are mostly attached, all the methods provide accurate prediction. Figure 18b shows the comparison of the proposed hierarchical method with the two RANS models. Our simulation switches to the SA RANS mode and gets a similar results to that of the RANS models, but produces a satisfactory prediction of axial velocity and flow angle. The  $k - \omega$  RANS model still overpredicts the turbulence intensity in the wake. Resolved turbulence is not available in the LES-RANS simulation as the SA model is used at this span location. Overall, the developed hierarchical modeling is able to provide a high-fidelity level of accuracy, outperforming the RANS methods.

As shown above, the hierarchical turbulence modelling employs high-fidelity LES in the region where low-fidelity RANS fails while retaining RANS in the region where it is capable. The computational cost is reduced by this zonalisation, compared with global high-fidelity simulations. To illustrate this point, the grid requirements and the estimated total grid numbers are compared in Table 2 for full-span fan simulations of different fidelity levels at the same operating point, where  $Re_c \approx 2 \times 10^6$ . For this wall bounded flow, the grid requirement is demanding for the inner part of boundary layer to resolve tiny near-wall structures, whose sizes are proportional to the viscous wall scale  $\delta_v = \nu/u_\tau$ , especially within viscous sublayer and buffer layer. Hence, the near-wall grid sizes are given in the wall unit, normalised by  $\delta_v$ , and the wall normal grid number given under  $d_w^+ = 10$ . These grid requirements are adapted from the Table 5.2 of the book written by Tucker [18] onto this case. The grid requirements of wall-modelled LES are refined by considering turbulence scales in both inner and outer parts of boundary layer. The total grid numbers for each type of simulation are estimated based on meshing the fan with entire hexahedral cells without hanging nodes. The estimated grid numbers are compared with that of current zonalised LES (ZLES), 63 million, by showing their ratios.

DNS of this fan configuration will require 3 orders magnitude larger grid number than that of the ZLES, as it resolves down to the dissipation range for the smallest turbulence scale, Kolmogorov scales. This makes DNS almost impossible to achieve for this case with current computational power. LES reduces this cost by targeting only the energetic scales. It decreases the grid number to 5-19.2 billion for this fan simulation, but it is still prohibitively expensive and 2 orders larger than the ZLES. It is because the majority of the LES grids are spent to resolve energy-containing eddies in the inner part of boundary layer, whose size scales with wall distance. However, the number of cells to resolve the outer-layer eddies, whose size scales with the boundary layer thickness  $\delta$ , is modest. This difference becomes significant at high Reynolds numbers. As noted for turbomachinery simulations, the grid count required to solve the inner part of boundary layer is dominant when  $Re_c$  is beyond  $1 \times 10^6$  [25], as the eddy sizes in inner and outer layers leading to different exponents of  $Re_c$  scaling, *i.e.*  $Re_c^{13/7}$  for  $d_w^+ < 100$  and  $Re_c^1$  for  $d_w^+ > 100$  [26]. To further mitigate the cost, the inner

part of the boundary layer can be modeled instead of resolved. The wall modelled LES (WMLES) was introduced in this spirit with only outer layer resolved but inner layer modelled. The WMLES near-wall grid requirements in Table 2 are estimated under the condition where the first grid point from the wall is at  $d_w^+ = 100$  and  $Re_\tau = \delta/\delta_v$  is 3000. The lower limit of near-wall grid sizes,  $\Delta s^+$  and  $\Delta r^+$ , corresponds to fine resolution of log-layer eddies [27], whose size still scales with wall distance, and the upper limit is for coarse resolution of the outer layer eddies [26]. As a result, the WMLES grid number is reduced to 0.12-5.72 billion, which has been one order of magnitude smaller than that of wall resolved LES (WRLES).

The grid number can be further reduced by zonalising WMLES in the separated flow region but without any adverse effects on accuracy. This leads to our ZLES method. The ZLES belongs to the category of hybrid LES-RANS, but it is different from the traditional type of hybrid methods, *i.e.* (D)DES [5]. First, instead of applying the same modelling strategy globally across the whole span, we zonally employ WMLES with RANS-based wall modelling only in the upper half span while using entire RANS in the lower half span. Second, RANS is only used under  $d_w^+ \approx 100$  as a wall model in the LES zone, in contrast to the (D)DES method where RANS covers the whole boundary layer, up to  $d_w^+ \sim o(1000)$ . The LES with a thin near-wall RANS layer is close to WMLES and expected to better capture non-equilibrium turbulence inside boundary layer for curvature-induced separation. Third, the transition between LES and RANS is achieved by blending the modelled turbulent stress  $\tau_{ij}^{turb}$  in ZLES rather than comparing the modelled turbulence length with grid size in (D)DES. This helps to reduce the extent of 'grey' area [28]. For our ZLES, the grid resolution used in the LES zone is higher than that of the (D)DES, because the outer boundary layer is resolved rather than modelled. It is close to the lower resolution limit of WMLES in Table 1, so the total grid number is approximately half of a full-span WMLES with the same resolution. For the DES-type simulation where only separated shear layers are resolved, the lowest required grid number is about 80 million if it is used globally across the whole span. This grid number is still 1.3 times of that of our current ZLES, as shown in Table 2. It is worth noting that our hierarchical turbulence modelling is a flexible framework that also allows (D)DES zonalised in half span to further reduce the cost, but WMLES was used here instead of (D)DES to ensure accuracy.

Overall, the ZLES makes the eddy resolving simulation of this fan rig affordable compared with DNS and WRLES, while achieving similar accuracy of WMLES with only half of its grid number. In addition, our hierarchical geometry modelling employs low-fidelity IBMfg for downstream stators. This further decreases the computational cost for the fan stage simulation if the interest is only in fan wakes. A stator passage of both the core and bypass ducts will require approximately the same amount of mesh cells as that was used in one fan rotor passage. For this configuration whose rotor-to-stator number ratio is about 1:2, the fan stage computational cost will triple that shown in Table 2, if the downstream stators are geometry-meshed and eddy-resolved in comprehensive high-fidelity way. For low-fidelity IBMfg, the cost of modelling downstream stators is almost negligible compared to that of the rotor passage simulation. This enables the fan stage simulation, accounting for the mean effects of downstream stators, at a cost close to that of the

**Table 2 Computational grid requirements and grid number estimate of full-span fan passage simulations**

Method	$\Delta s^+/\min(\Delta d_w^+)/\Delta r^+$	$N_{grid}$ for $d_w^+ < 10$	Total $N_{grid,est}$ , million	$\frac{N_{grid,est}}{N_{grid,ZLES}}$
DNS	(10-15)/1/5	3-5	192,000-288,000	3048-4571
Wall Resolved LES	(50-130)/1/(15-30)	3-5	5,000-19,200	79-305
Wall Modeled LES	(60-600)/(30-150)/(40-200)	0	120-5,720	1.9-90.8
(D)DES	(100-600)/1/(100-300)	2-5	80-1,440	1.3-22.9
RANS	(500-1000)/1/(100-1000)	2-5	0.7-1.5	0.011-0.024

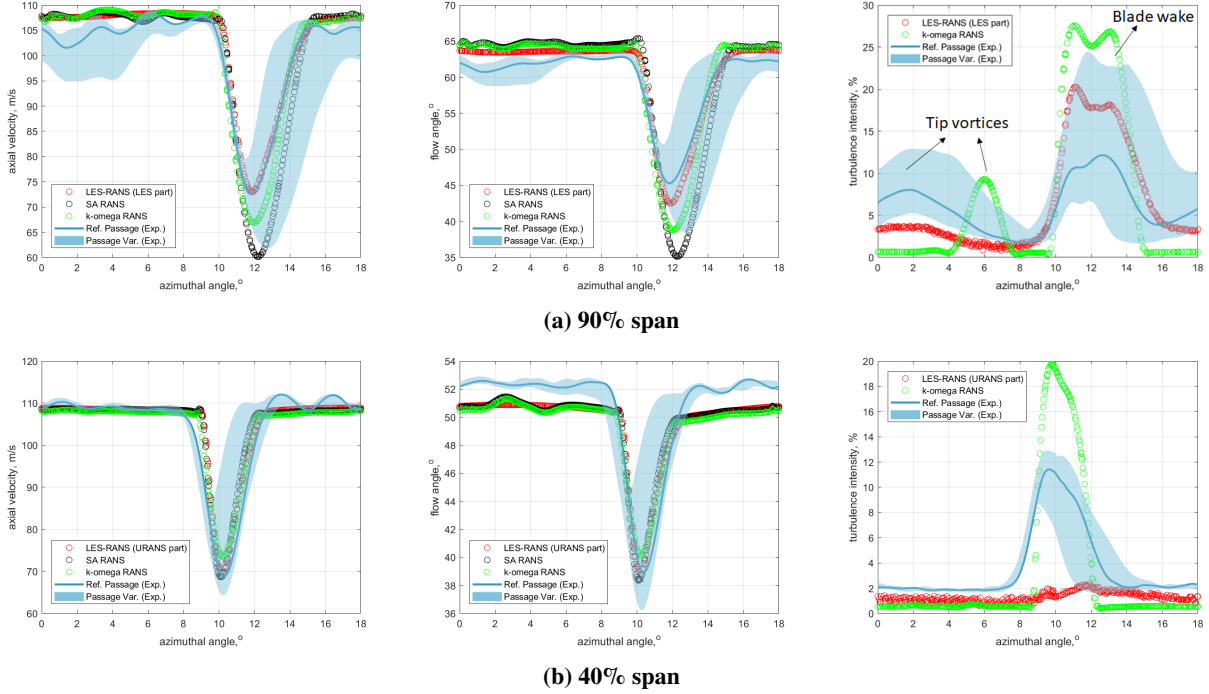


**Fig. 18 LES-RANS and RANS predictions of azimuthal wake profiles of axial velocity, flow angle and turbulent intensity at the 90% and 40% span locations in the interstage measurement plane downstream of the fan rotor**

rotor-alone simulation. It is also worth noting that, compared with our project partners' stage simulation - 1 rotor and 2 stators, our mesh number is about 0.17 of fine-grid ZDES [21] and 0.47 of coarse-grid WMLES [20], although the grid resolutions of the three types of simulations are different. Compared to the other two, our ZLES grid resolution in the upper span is in-between.

## F. Wake turbulence analysis

In addition to the accurate prediction of flow statistics, hierarchical modelling also provides eddy-resolved and time-accurate solutions to assess the assumptions made in the low-order models of fan broadband noise. Fan broadband noise is primarily generated by the interactions of fan turbulent wake with the downstream stators. One key assumption made in fan broadband noise models is that the wake turbulence is isotropic [29], and the velocity spectra can be

obtained using energy spectrum model proposed by Von Karman [30], given the turbulence intensity and the integral length scale. Therefore, the LES results in the upper half span are used to assess the isotropic turbulence assumption.

### 1. Turbulence anisotropy

The state of turbulence anisotropy can be characterised using two independent invariants  $\eta$  and  $\zeta$  of the Reynolds-stress anisotropy tensor  $b_{ij}$  [31]. The two invariants are defined as

$$\eta = \sqrt{\frac{b_{ij}b_{ij}}{6}} \quad (9)$$

$$\zeta = \sqrt{\frac{b_{ij}b_{jk}b_{ki}}{6}} \quad (10)$$

where the anisotropy tensor is written as  $b_{ij} = \frac{\langle u'_i u'_j \rangle}{u'_i u'_i} - \frac{1}{3} \delta_{ij}$ .

Figure 19 shows the Lumley triangle on the plane of  $\zeta$  and  $\eta$ . The turbulence state is only realisable within this triangle. The three points on the triangle is corresponding to three distinct turbulence states. The bottom point (ISO) refers to the isotropic state, while the upper left point (1C) represents the one-component anisotropic state where the turbulent fluctuation is just in one direction, and the upper right point (2C) refers to the two-component anisotropic state, where the turbulent fluctuations are isotropic in two dimensions with the third component equal to zero. The turbulent wake downstream the fan blade is characterised on this  $\zeta - \eta$  plane. Each scatter point represents the turbulent state at one spatial location. Figure 19a shows the wake anisotropy state at 70% span plane coloured by the axial distance from the fan blade trailing edge. It spreads out towards 1C state near the trailing edge, because of the strong shear and wall-normal restriction. As the wake develops downstream, it moves towards the isotropic state and the shape of Reynolds-stress ellipsoid stays close to prolate sphere which is the 1C-ISO line. This indicates that the shear-direction fluctuation is larger than the other two, but the other two direction fluctuations are at a similar level. If the wake centre, where the minimum axial velocity is located, is selected and plotted in Fig. 19b, the turbulence is much closer to isotropic except the points near the blade trailing edge. After showing the axial variation of wake turbulence anisotropy, we further investigate its radial variation. Figure 19c shows that the anisotropy state of scatter points coloured by their radial locations on the  $x/c = 0.42$  plane where the predicted wake profile were compared with the experimental measurements. In general, the points are near the right line of Lumley triangle, indicating the fluctuations are larger in the shear direction. As moving from the middle span to the tip region, the points are spreading towards the upper line of Lumley triangle, indicating that the casing introduces more anisotropy by reducing fluctuations in the wall normal direction. It is worth noting that the scattering of the same colour points in Figures 19a and 19c are caused by the their azimuthal position. To illustrate the azimuthal variation of turbulence anisotropy across the wake, Fig. 19d shows one example at 70% span. This is corresponding to the wake velocity profile in Fig. 12c and the velocity fluctuations in Fig. 13c. The turbulence starts from the isotropic state in main stream, and increases anisotropy across the wake, with a peak



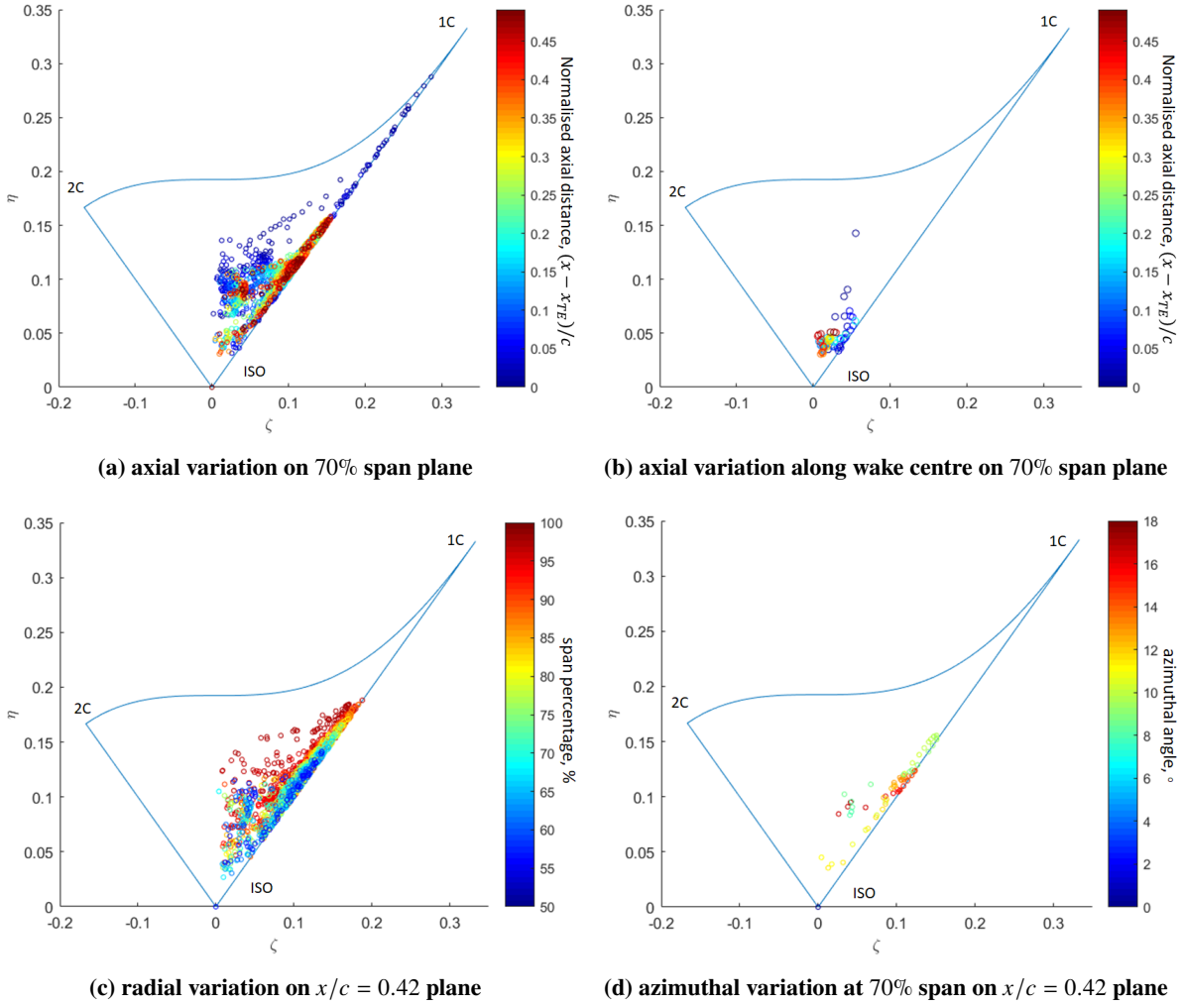


**Fig. 19** Anisotropy characterisation of fan wake turbulence on the plane of two independent invariants  $\zeta$  and  $\eta$  of Reynolds Stress. 1C, one-component state; 2C, two-component state; iso, isotropic state

near the half-width position of the wake, 10 degrees and 14 degrees, and then decreases towards isotropic in the wake centre.

In summary, the fan wake becomes more isotropic when developing downstream. Across the wake, the most anisotropic turbulent state occurs at around the half wake width where the largest shear is present, while the turbulence at the wake centre is close to isotropic. In addition, the anisotropy increases towards blade and endwall due to the wall restriction.

## 2. Velocity spectra

In addition to the assessment of the wake turbulence's anisotropy, the validity of the velocity spectrum model is further examined. The model spectra of turbulence kinetic energy is still based on the isotropic turbulence assumption and can be described analytically. In this paper, the Von Karman spectrum model [30] is used for describing the 3D

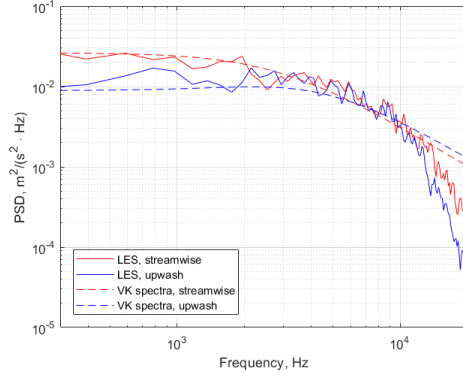
kinetic energy spectra and the 1D longitudinal and transversal velocity spectra [32, 33] are derived by integrating it over the other two dimensions. The 1D velocity spectra can be directly compared with the power spectra density of our LES data by converting streamwise wave number  $k_c$  to frequency  $f = U_c k_c$  using Taylor's frozen eddy hypothesis.

Corresponding to the velocities and their fluctuations in Figures 12 and 13, some typical locations on the same axial plane are selected to evaluate how well their velocity spectra can be modeled using Von Karman's energy spectrum. As the Amiet-based acoustic model [32] takes the downstream stator as a radial stack of 2D airfoils, the velocity is transformed into the cylindrical coordinates and the velocity fluctuations are decomposed into streamwise and upwash directions. The upwash direction is perpendicular to the blade chord direction on the radial plane. The blade chord direction can be approximated by the mean flow direction if the angle of attack is small. Upwash velocity spectra are important for noise prediction, as the Amiet model directly takes them as input to compute rotor-stator interaction noise at each radial location.

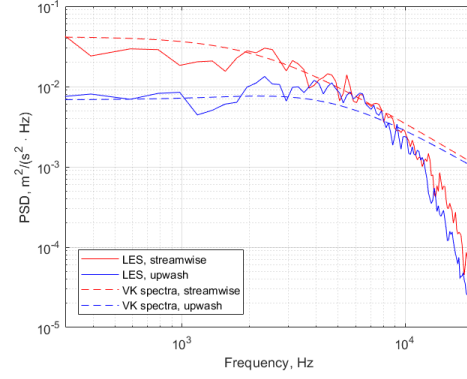
Figure 20 shows the streamwise and upwash velocity spectra at a few typical locations inside the wake, *i.e.* wake centre and half-width positions. The LES velocity spectra are plotted against those calculated by Von Karman spectrum model. To obtain the Von Karman spectra, the integral length scales and turbulent fluctuation amplitude are computed using LES data for both streamwise and upwash velocities as the model input. In general, the Von Karman are in a reasonable agreement with the LES spectra before  $10^4$  Hz where the LES spectra is numerically cut off. In the wake centre, as discussed in the previous section, the turbulence state is close to the isotropic state, so the Von Karman spectra show a great capability of reproducing the LES spectra. Moving from blade tip to middle span, the low-frequency difference between streamwise and upstream velocity spectra become small, also indicating that the turbulence is more isotropic towards the middle span. As shown in Fig. 19d, the anisotropy peaks at the wake half-width location near the blade pressure side. However, the model spectra still shows a surprising agreement with the LES spectra. This is partly because the fluctuation amplitude and length scale of each velocity component is calculated using LES data, which takes certain degree of anisotropy into account. This indicates that the Von Karman spectrum model of isotropic turbulence can still be used to describe the wake velocity spectra given the proper fluctuation amplitudes and length scales, despite the anisotropy in the wake turbulence.

## IV. Conclusion

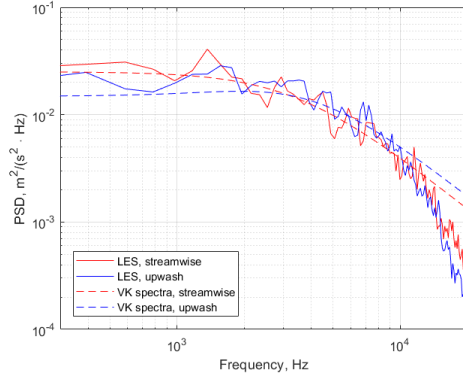
Challenges are faced to simulate coupled fluid systems with complex geometry and turbulence. A modelling hierarchy of turbulence and geometry is explored in this paper to reduce the computational effort. In the developed hierarchical modelling approach, the flow and geometry can be treated zonally at various fidelity levels. The method has been successfully applied to a fan stage with bypass configuration. The fan operated at half of the design speed, leading to excessive separation in the tip region. For turbulence modelling, LES is zonalised in the upper half span to predict the separated flow and the tip leakage, while RANS is used to simulate the relatively clean hub flow. For geometry



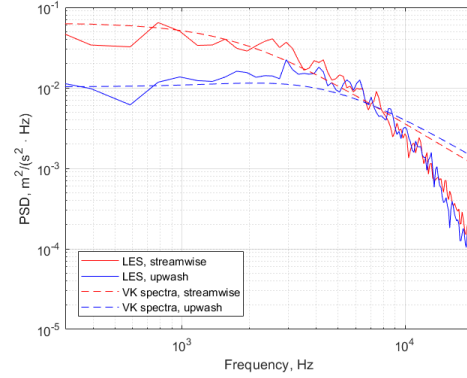
(a) wake centre at 90% span



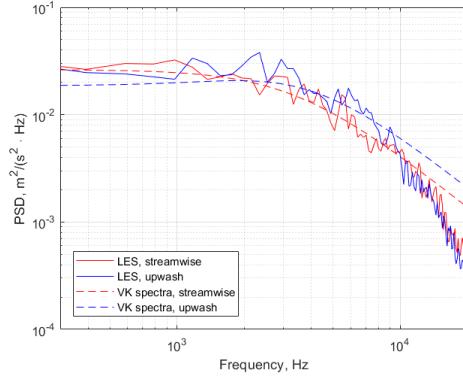
(b) pressure-side wake half width at 90% span



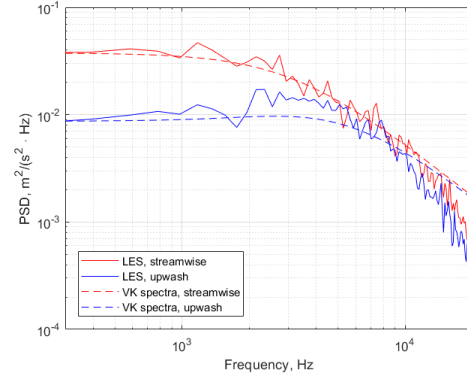
(c) wake centre at 80% span



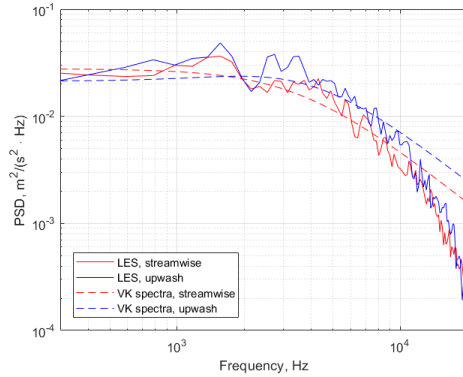
(d) pressure-side wake half width at 80% span



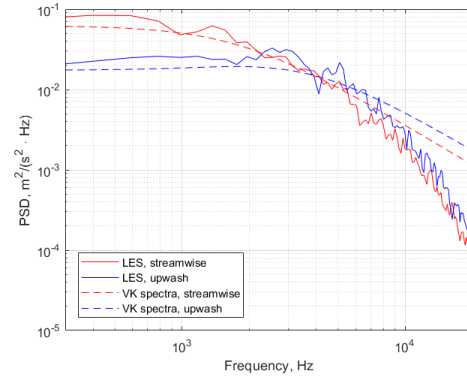
(e) wake centre at 70% span



(f) pressure-side wake half width at 70% span



(g) wake centre at 60% span



(h) pressure-side wake half width at 60% span

Fig. 20 Comparison of LES velocity spectra with Von Karman (VK) spectra in the fan wake at  $x/c = 0.42$  plane

modelling, the fan blade is resolved by grids while the downstream stators are modelled using low-order IBMfg, where the stator geometry is filtered by imposing azimuthally homogeneous body forces. The accurate simulation has been obtained with 63 million cells using this proposed hierarchical modelling strategy, while a proper wall-resolved LES will require 5-19.2 billion cells to fulfill the same task. In the simulation, fine-scale turbulence is well resolved in the LES zone and a smooth transition is achieved into the RANS region where ensemble-averaged large-scale flow motions are recovered. The simulation has been systematically compared with experimental measurements at the interstage. Overall, high accuracy is achieved by this hierarchical modelling. In the upper half span, the LES is compared with the measurements in terms of the mean velocities and the turbulent fluctuations. The LES shows a satisfactory agreement with the measurements in the reference passage and within the passage-to-passage variation. In the lower half span, wake profiles are also predicted by RANS with the expected accuracy. The sensitivity of the radial RANS-LES interface has been tested and shows minimal effects on the overall flow prediction. The simulation results have been briefly exploited to assess the isotropic turbulence assumptions that are made on turbulent fan wake in low-order fan broadband noise models. It is found that the wake shows strong anisotropy at the wake half-width position, however, the velocity spectrum shape can still be reasonably captured by the Von Karman's isotropic turbulence spectra, given appropriate fluctuation amplitudes and integral length scales. In the future, the simulation data will be further explored to assess fan wake modelling assumptions and investigate the underlying mechanisms of fan tip noise generation.

## Acknowledgments

The work is funded in the EU H2020 project “TurboNoiseBB” under grant agreement No. 690714. The authors would like to thank the computational time made provided via the UK turbulence consortium by the EPSRC grant EP/R029326/1 on the UK supercomputing facility ARCHER2 and also by the EPSRC RAP project cs053 on Tier-2 machine CSD3 at Cambridge.

## References

- [1] Slotnick, J. P., Khodadoust, A., Alonso, J., Darmofal, D., Gropp, W., Lurie, E., and Mavriplis, D. J., “CFD vision 2030 study: a path to revolutionary computational aerosciences,” Technical Report NASA/CR-2014-218178, National Aeronautics and Space Administration, 2014.
- [2] Chawner, J. R., and Taylor, N. J., “Progress in Geometry Modeling and Mesh Generation Toward the CFD Vision 2030,” *AIAA Paper 2019-2945*, June 2019. <https://doi.org/10.2514/6.2019-2945>.
- [3] Mittal, R., and Iaccarino, G., “IMMERSED BOUNDARY METHODS,” *Annual Review of Fluid Mechanics*, Vol. 37, No. 1, 2005, pp. 239–261. <https://doi.org/10.1146/annurev.fluid.37.061903.175743>.
- [4] Cao, T., Hield, P., and Tucker, P. G., “Hierarchical Immersed Boundary Method with Smeared Geometry,” *Journal of Propulsion and Power*, Vol. 33, No. 5, 2017, pp. 1151–1163. <https://doi.org/10.2514/1.B36190>.

- [5] Spalart, P. R., "Detached-Eddy Simulation," *Annual Review of Fluid Mechanics*, Vol. 41, No. 1, 2009, pp. 181–202. <https://doi.org/10.1146/annurev.fluid.010908.165130>.
- [6] Deck, S., "Recent improvements in the zonal detached eddy simulation (ZDES) formulation," *Theoretical and Computational Fluid Dynamics*, Vol. 26, No. 6, 2012, pp. 523–550. <https://doi.org/10.1007/s00162-011-0240-z>.
- [7] Holgate, J., Skillen, A., Craft, T., and Revell, A., "A review of embedded large eddy simulation for internal flows," *Archives of Computational Methods in Engineering*, Vol. 26, No. 4, 2019, pp. 865–882. <https://doi.org/10.1007/s11831-018-9272-5>.
- [8] He, L., "Averaging for High Fidelity Modeling—Toward Large Eddy Simulations in Multi-Passage Multi-Row Configurations," *Journal of Turbomachinery*, Vol. 143, No. 2, 2021. <https://doi.org/10.1115/1.4049616>, URL <https://doi.org/10.1115/1.4049616>, 021002.
- [9] Ma, Y., Cui, J., Vadlamani, N. R., and Tucker, P., "Effect of Fan on Inlet Distortion: Mixed-Fidelity Approach," *AIAA Journal*, Vol. 56, No. 6, 2018, pp. 2350–2360. <https://doi.org/10.2514/1.J056858>.
- [10] Ma, Y., Cui, J., Vadlamani, N. R., and Tucker, P., "Hierarchical geometry modelling using the immersed boundary method," *Computer Methods in Applied Mechanics and Engineering*, Vol. 355, 2019, pp. 323–348. <https://doi.org/10.1016/j.cma.2019.06.019>.
- [11] Ubald, B. N., Watson, R., Cui, J., Tucker, P., and Shahpar, S., "Application of an Immersed Boundary Method on an Instrumented Turbine Blade With Large Eddy Simulation," *Journal of Turbomachinery*, Vol. 143, No. 11, 2021. <https://doi.org/10.1115/1.4051110>.
- [12] Tucker, P. G., and Wang, Z. N., "Eddy Resolving Strategies in Turbomachinery and Peripheral Components," *Journal of Turbomachinery*, Vol. 143, No. 1, 2021. <https://doi.org/10.1115/1.4048697>, 010801.
- [13] Nicoud, F., and Ducros, F., "Subgrid-scale stress modelling based on the square of the velocity gradient tensor," *Flow, turbulence and Combustion*, Vol. 62, No. 3, 1999, pp. 183–200. <https://doi.org/10.1023/A:1009995426001>.
- [14] Spalart, P., and Allmaras, S., "A one-equation turbulence model for aerodynamic flows," *AIAA Paper 1992-439*, January 1992. <https://doi.org/10.2514/6.1992-439>.
- [15] Cao, T., Vadlamani, N. R., Tucker, P. G., Smith, A. R., Slaby, M., and Sheaf, C. T. J., "Fan–Intake Interaction Under High Incidence," *Journal of Engineering for Gas Turbines and Power*, Vol. 139, No. 4, 2016. <https://doi.org/10.1115/1.4034701>, 041204.
- [16] Cui, J., Watson, R., Ma, Y., and Tucker, P., "Low Order Modeling for Fan and Outlet Guide Vanes in Aero-Engines," *Journal of Turbomachinery*, Vol. 141, No. 3, 2019. <https://doi.org/10.1115/1.4042202>, 031002.
- [17] Jameson, A., "Formulation of kinetic energy preserving conservative schemes for gas dynamics and direct numerical simulation of one-dimensional viscous compressible flow in a shock tube using entropy and kinetic energy preserving schemes," *Journal of Scientific Computing*, Vol. 34, No. 2, 2008, pp. 188–208. <https://doi.org/10.1007/s10915-007-9172-6>.

- [18] Tucker, P. G., *Advanced Computational Fluid and Aerodynamics*, Cambridge Aerospace Series, Cambridge University Press, 2016. <https://doi.org/10.1017/CBO9781139872010>.
- [19] Meyer, R. K., Hakansson, S., Hage, W., and Enghardt, L., “Instantaneous flow field measurements in the interstage section between a fan and the outlet guiding vanes at different axial positions,” *Proc. of 13th European Conference on Turbomachinery Fluid dynamics & Thermodynamics*, 2019, pp. ETC2019–330. <https://doi.org/10.29008/ETC2019-330>.
- [20] Lewis, D., Moreau, S., Jacob, M. C., and Sanjosé, M., “ACAT1 Fan Stage Broadband Noise Prediction Using Large-Eddy Simulation and Analytical Models,” *AIAA Journal*, 2021. <https://doi.org/10.2514/1.J060163>.
- [21] François, B., Barrier, R., and Polacsek, C., “Zonal Detached Eddy Simulation of the Fan-OGV Stage of a Modern Turbofan Engine,” 2020. <https://doi.org/10.1115/GT2020-14239>, v02AT32A004.
- [22] Polacsek, C., Daroukh, M., François, B., and Barrier, R., “TURBOFAN BROADBAND NOISE PREDICTIONS BASED ON A ZDES CALCULATION OF A FAN-OGV STAGE,” *Forum Acusticum 2020*, Lyon, France, 2020. <https://doi.org/10.48465/fa.2020.0032>, URL <https://hal.archives-ouvertes.fr/hal-03181349>.
- [23] Menter, F. R., “Two-equation eddy-viscosity turbulence models for engineering applications,” *AIAA Journal*, Vol. 32, No. 8, 1994, pp. 1598–1605. <https://doi.org/10.2514/3.12149>.
- [24] Laborderie, H. d., and Nodé-Langlois, T., “Assessment of WP4 fan stage broadband noise advanced prediction methods,” Technical Report D2.5, TurboNoiseBB Consortium, 2020.
- [25] Tucker, P., Eastwood, S., Klostermeier, C., Jefferson-Loveday, R., Tyacke, J., and Liu, Y., “Hybrid LES Approach for Practical Turbomachinery Flows—Part I: Hierarchy and Example Simulations,” *Journal of Turbomachinery*, Vol. 134, No. 2, 2011. <https://doi.org/10.1115/1.4003061>.
- [26] Choi, H., and Moin, P., “Grid-point requirements for large eddy simulation: Chapman’s estimates revisited,” *Physics of Fluids*, Vol. 24, No. 1, 2012, p. 011702. <https://doi.org/10.1063/1.3676783>.
- [27] “Grid requirements for wall-stress modelled LES,” <https://wmles.umd.edu/wall-stress-models/grid-requirements/>, September 2022.
- [28] Menter, F., “Stress-Blended Eddy Simulation (SBES)—A New Paradigm in Hybrid RANS-LES Modeling,” *Progress in Hybrid RANS-LES Modelling*, edited by Y. Hoarau, S.-H. Peng, D. Schwaborn, and A. Revell, Springer International Publishing, Cham, 2018, pp. 27–37. [https://doi.org/10.1007/978-3-319-70031-1\\_3](https://doi.org/10.1007/978-3-319-70031-1_3).
- [29] Guérin, S., Kissner, C., Seeler, P., Blázquez, R., Carrasco Laraña, P., de Laborderie, H., Lewis, D., Chaitanya, P., Polacsek, C., and Thisse, J., “ACAT1 Benchmark of RANS-Informed Analytical Methods for Fan Broadband Noise Prediction: Part II—Influence of the Acoustic Models,” *Acoustics*, Vol. 2, MDPI, 2020, pp. 617–649. <https://doi.org/10.3390/acoustics2030033>.
- [30] Von Karman, T., “Progress in the statistical theory of turbulence,” *Proceedings of the National Academy of Sciences*, Vol. 34, No. 11, 1948, pp. 530–539. <https://doi.org/10.1073/pnas.34.11.530>.

- [31] Pope, S. B., and Pope, S. B., *Turbulent flows*, Cambridge university press, 2000. <https://doi.org/doi:10.1017/CBO9780511840531>.
- [32] Amiet, R., “Acoustic radiation from an airfoil in a turbulent stream,” *Journal of Sound and Vibration*, Vol. 41, No. 4, 1975, pp. 407–420. [https://doi.org/https://doi.org/10.1016/S0022-460X\(75\)80105-2](https://doi.org/https://doi.org/10.1016/S0022-460X(75)80105-2), URL <https://www.sciencedirect.com/science/article/pii/S0022460X75801052>.
- [33] Wilson, D. K., “Three-Dimensional Correlation and Spectral Functions for Turbulent Velocities in Homogeneous and Surface-Blocked Boundary Layers.” Tech. rep., ARMY RESEARCH LAB ADELPHI MD, 1997.